Structure

Molecular Mechanism of Dopamine Transport by Human Dopamine Transporter

Graphical Abstract

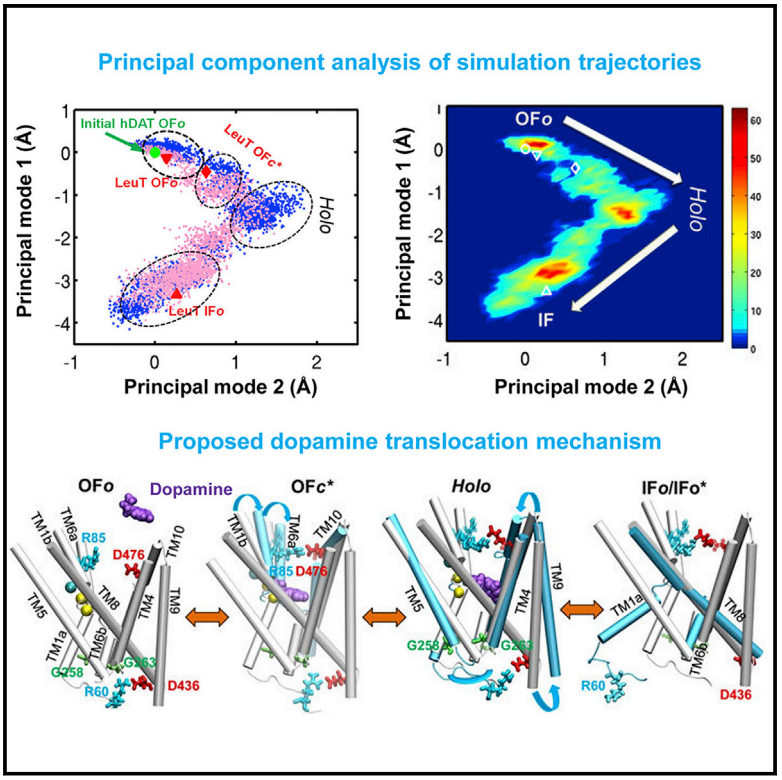

Highlights

- DA binding from the extracellular (EC) region prompts the closure of two EC gates
- Intermediate state occluded to both EC and intracellular (IC) regions is identified
- Dislocation of Na2 triggers the transition to substrate-releasing state
- A redistribution of IC-facing salt bridges stabilizes the inward-facing state

Authors

Mary Hongying Cheng, Ivet Bahar

Correspondence

bahar@pitt.edu

In Brief

Using advanced molecular modeling, Cheng and Bahar present a comprehensive account of dopamine translocation through human dopamine transporter at the atomic level. The study provides a first structural model for a substrate/ion-bound occluded (*holo-occluded*) state transiently stabilized during the transport process.

Cheng & Bahar, 2015, Structure *23*, 2171–2181
November 3, 2015
http://dx.doi.org/10.1016/j.str.2015.09.001

Structure
Theory

Molecular Mechanism of Dopamine Transport by Human Dopamine Transporter

Mary Hongying Cheng[1] and Ivet Bahar[1,*]
[1]Department of Computational and Systems Biology, School of Medicine, University of Pittsburgh, 3064 Biomedical Science Tower 3, 3501 Fifth Avenue, Pittsburgh, PA 15260, USA
*Correspondence: bahar@pitt.edu
http://dx.doi.org/10.1016/j.str.2015.09.001

SUMMARY

Dopamine transporters (DATs) control neurotransmitter dopamine (DA) homeostasis by reuptake of excess DA, assisted by sodium and chloride ions. The recent resolution of DAT structure (dDAT) from *Drosophila* permits us for the first time to directly view the sequence of events involved in DA reuptake in human DAT (hDAT) using homology modeling and full-atomic microseconds accelerated simulations. Major observations are spontaneous closure of extracellular gates prompted by DA binding; stabilization of a *holo-occluded* intermediate; disruption of N82-N353 hydrogen bond and exposure to intracellular (IC) water triggered by Na2 dislocation; redistribution of a network of salt bridges at the IC surface in the inward-facing state; concerted tilting of IC-exposed helices to enable the release of Na^+ and Cl^- ions; and DA release after protonation of D79. The observed time-resolved interactions confirm the conserved dynamics of LeuT-fold family, while providing insights into the mechanistic role of specific residues in hDAT.

INTRODUCTION

Human dopamine transporter (hDAT) belongs to the family of neurotransmitter:sodium symporters (NSS), which includes serotonin, norepinephrine, and γ-aminobutyric acid transporters. Malfunction of hDAT has been implicated in many neurological and psychiatric disorders, such as attention-deficit hyperactivity disorder, bipolar disorder, clinical depression, drug addiction, and alcoholism (Vaughan and Foster, 2013; Amara and Sonders, 1998), and hDAT is an important target for therapeutic antidepressants.

The specific mechanism of function of DAT at the atomic scale has been elusive to date due to lack of structural data. With the elucidation of the first DAT structure (from *Drosophila melanogaster*; dDAT) in 2013 (Penmatsa et al., 2013), and the recent dDAT structures in the presence of dopamine, cocaine, and amphetamine (Wang et al., 2015), we now have access to valuable data for structure-based explorations of DAT's mechanism of function.

In the absence of structural data for DAT, information on the dynamics of hDAT at the atomic scale has been inferred from models or simulations based on the bacterial transporter LeuT (Beuming et al., 2006; Gedeon et al., 2010; Indarte et al., 2008; Kniazeff et al., 2008; Guptaroy et al., 2009; Huang and Zhan, 2007). DAT shares the same fold as LeuT, which has long served as a prototype for understanding the mechanism of function of LeuT-fold family members, being the first member of that family structurally resolved (Yamashita et al., 2005) and characterized in multiple states (Krishnamurthy and Gouaux, 2012; Piscitelli et al., 2010; Singh et al., 2008). Computational studies performed for NSS family members that share the LeuT fold (Kantcheva et al., 2013; Cheng and Bahar, 2013, 2014; Khafizov et al., 2012; Shaikh and Tajkhorshid, 2010; Zomot and Bahar, 2012; Thomas et al., 2012; Stockner et al., 2013; Zomot et al., 2015) also helped understand the structural and dynamic features of the family, e.g. the organization of the 12 transmembrane (TM) helices (TM1–TM12) in two pseudo-symmetric inverted repeats (Forrest, 2013; Forrest et al., 2008; Forrest and Rudnick, 2009), or the complex coupling between global and local structural transitions during substrate transport (Cheng and Bahar, 2013). Global transitions take place between outward-facing (OF) and inward-facing (IF) states, in line with the classical alternating-access model (Jardetzky, 1966); local conformational switches control the opening/closure of the extracellular (EC) or intracellular (IC) gates in the respective OF or IF states (Cheng and Bahar, 2013). The resolution of dDAT, which has more than 50% sequence identity with hDAT (as opposed to 22% between LeuT and hDAT [Stockner et al., 2013]), as well as the identification of the binding sites of two sodium ions (Na1 and Na2) and a chloride ion in the dDAT crystal, present an excellent starting point for investigating dopamine (DA) transport mechanism at the atomic scale and comparing it with (and consolidating) earlier work, as indicated by our recent examination (Cheng et al., 2015) of the binding properties of different psychostimulants on hDAT.

The conformational events that mediate substrate/ion transport occur over a broad range of time scales (from nanoseconds to beyond milliseconds). Visualization of local events requires atomic models and molecular dynamics (MD) simulations, but global motions cannot be captured by conventional MD. Instead, multiscale methodologies are needed. A powerful method is accelerated MD (aMD) (Hamelberg et al., 2004) which, combined with conventional MD (cMD) and targeted MD (Shaikh and Tajkhorshid, 2010), helped us elucidate the substates visited along the LeuT transport cycle (Cheng and Bahar, 2014):

OF*o* → OF*c** → *holo-occluded* → IF*o** → IF*o* → *apo-occluded*

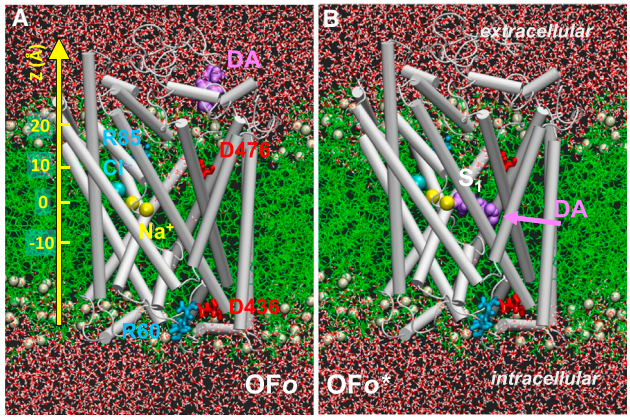

Figure 1. Initial Setup for Two Sets of Simulations

hDAT is in the outward-facing open (OF*o*) state, with the ligand (DA; purple, space-filling) either in the EC region (OF*o*; A), or bound to the site S_1 (OF*o**; B). The EC gate R85-D476 is open, and the IC gate R60-D436 is closed. The POPC lipids are shown as green lines with P-atoms as tan spheres; water molecules are in red/white. Cyan and yellow spheres represent the Cl^- and two Na^+ ions detected in the dDAT structure (PDB: 4M48). (A) shows the z scale used in assessing the position of substrate and ions during their translocation.

Here the asterisk designates the substrate/ion-bound state, and suffixes *o* and *c* refer to the *open* or *closed* conformers of the EC or IC gates (e.g. OF*c** is the substrate-bound OF transporter with closed EC gate). Of these six computationally detected substates, three have been resolved for LeuT: OF*o* (Krishnamurthy and Gouaux, 2012), OF*c** (Yamashita et al., 2005), and IF*o* (Krishnamurthy and Gouaux, 2012). Recently, the first crystal structure of an occluded inward-facing state (IF*c**; comparable with *holo-occluded*) with bound Na^+ and substrate has been resolved for MhsT (Malinauskaite et al., 2014), another member of the NSS family.

In the present study, we implemented a dual-boost aMD (Hamelberg et al., 2007; Miao et al., 2013) and cMD to study the mechanism of function of hDAT. We observe not only the conformational switches at the gate residues, but also the global structural transitions from OF*o* to IF*o* states. Our simulations elucidate the structure of hDAT at various stages of the translocation process, including DA-bound OF*c** state, which exhibits close resemblance to Leu-bound LeuT (Yamashita et al., 2005). They also support the existence of a temporarily stabilized *holo-occluded* state closed to both EC and IC environments (in lieu of occluded IF*c**) along the transport cycle of DAT. The simulations provide a clear picture of the sequence of events and key interactions that enable DA transport, starting from recognition and uptake from the synapse, all the way to the release to the cytosol.

RESULTS

Overview of Simulations

We performed two sets of simulations (Figure 1) starting from: (A) the OF*o* state with a DA molecule initially placed in the EC region more than 20 Å away from D79 at the EC vestibule; and (B) the same structure with a DA docked onto the primary substrate-binding site S_1 consistently detected in the first set of runs as well as independent docking simulations, designated as OF*o** (see Supplemental Information). The hDAT structure used for initiating the simulations was constructed (Cheng et al., 2015) by homology modeling (Sali and Blundell, 1993) using the dDAT structure as template. The simulations helped visualize the conformational fluctuations of *apo* hDAT in the OF*o* state (runs 1–2); the mechanism of DA recognition and binding (runs 3–6); hDAT reconfiguration into OF*c** state (runs 5–11); subsequent progression to *holo-occluded* (runs 5–6 and 9–11); opening of the IC vestibule to transition to IF*o** (runs 6, 9–11); and release of DA (runs 12–13). All reported events were verified to be reproduced in at least two runs. aMD runs 14–17 were performed for *apo* hDAT to verify that the closure of the EC vestibule was stabilized upon DA binding to site S_1, and not in the *apo* state. Table S1 gives a summary of all runs. Detailed methods, including the construction of the EL2 loop S190-P212 unresolved in dDAT, are presented in the Experimental Procedures.

Uptake of DA from the EC Region Involves a First Recognition Site

The first set of simulations revealed two sites involved in DA binding from the EC region (Figures 2 and S1): The first, located by DA within nanoseconds (cMD runs 3–4), was a recognition site (S_0) at the upper part of the EC vestibule; D79 and D476 coordinated the DA amine and carbonyl groups, respectively. The second, observed in extended aMD runs 5–6, was more buried into the vestibule, closely coinciding with the primary binding site S_1 identified for LeuT (Yamashita et al., 2005). DA stably located this site after transient binding to S_0 (see Movie S1). Figure 2 depicts the trajectory of DA and accompanying hDAT structural changes as DA proceeds from the EC region, to S_0, and to S_1: first, the R85-D476 salt bridge forms after DA binding to S_0, which serves as the outer EC gate that prevents its escape back to the EC medium; F320 (C_α-C_β dihedral angle χ_1) shows rotational isomeric fluctuations predisposing it to associate with Y156 (inner EC gate stabilized after DA binding to S_1).

Substrate Binding Prompts the Closure of Two EC Gates

In the majority of our simulations, the binding of DA to S_1 led to the closure of the EC gates R85-D476 (outer) and Y156-F320 (inner) within ~100 ns (Figure 3). A closer examination showed that the binding of DA, and in particular its attractive interaction with D79, disrupted a local network of hydrogen bonds that would form intermittently between D79, Y156, and N82 in the OF*o* state (prior to DA binding) (Figure S1). This freed Y156, which could then pair up with F320 in the isomeric state $\chi_1 = -160° \pm 15°$. Y156-F320 association occurred upon the DA-stimulated disruption of the original network of interactions. In the absence of DA binding (runs 1–4 and 14–16), the occasional jumps of F320 from its original (OF*o*) state ($\chi_1 = -75° \pm 15°$) to $\chi_1 = -160° \pm 15°$ were short-lived and the EC vestibule generally remained open. F320 is the counterpart of F253 in LeuT, whose isomerization and subsequent interaction with Y108 stabilizes the bound substrate (Cheng and Bahar, 2013). The DA-bound hDAT indeed ends up assuming a closed structure, OF*c**, remarkably similar to that of Leu-bound LeuT (Yamashita et al., 2005).

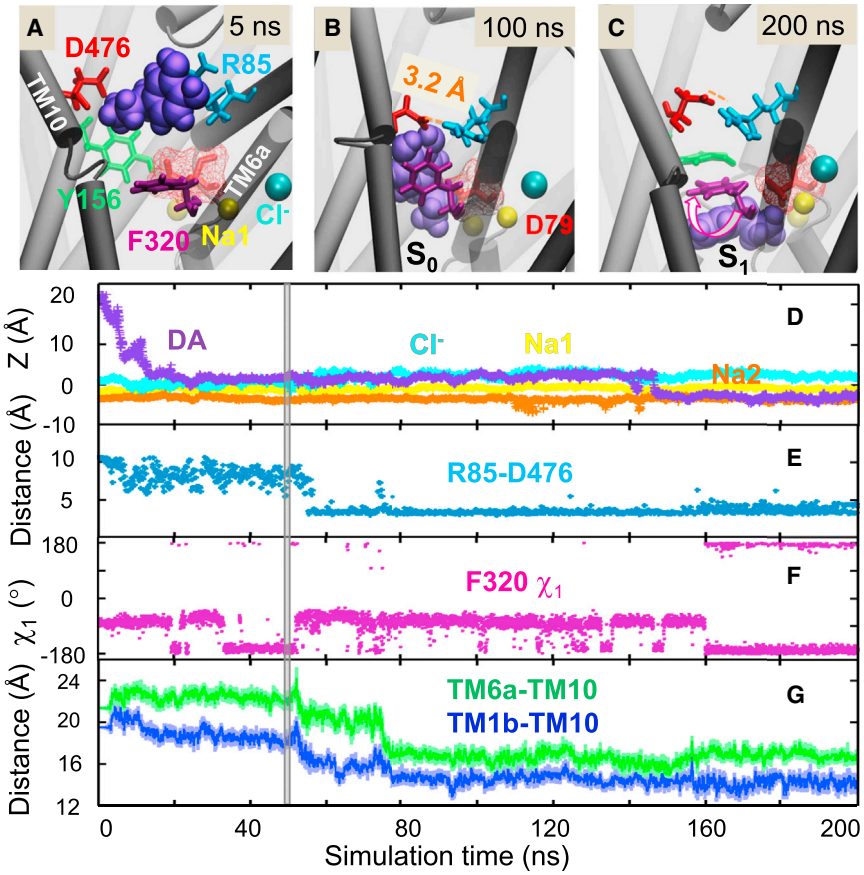

Figure 2. Dopamine Recognition and Permeation through the EC Vestibule and Binding to Site S_1, and Concurrent Conformation Changes in hDAT

(A–C) Positions of DA (purple van der Waals spheres) with respect to R85, D476, Y156, F320, and D79 (red stick with mesh), at 5, 100, and 200 ns.

(D) Time evolutions of z coordinates of DA, Na1, Na2, and Cl^- relative to D79 mass center.

(E) R85-D476 (outer EC gate) N-O distance. Salt bridge forms around 50 ns.

(F) χ_1 of F320, flips from $-75 \pm 15°$ to $\pm 180°$ around 160 ns.

(G) Center-of-mass distances of EC-exposed TM6a-TM10 and TM1b-TM10. Gray vertical bar marks the switch from cMD (run 3) to aMD (run 6). See also Figure S1.

In addition to these local conformational switches, DA binding was accompanied by global changes, mainly 10°–15° inward tiltings in TM1b and TM6a toward the center of the EC vestibule, coupled to the closure of the EC gates (Figures 2G and 3). Furthermore, TM10 broke near S422-G426, presumably to accommodate these rearrangements.

These global and local changes consistently led to the same conformer, OF*c**, with a root-mean-square deviation (RMSD) of 2.0 ± 0.2 Å, at the end of two independent cMD runs: one with Anton (Shaw et al., 2008) (2 μs, run 7) and the other with NAMD (Phillips et al., 2005) (100 ns, run 8; Table S1). The site S_1 was minimally hydrated with only three to four water molecules occasionally coordinating Na2 and DA. Figure S2 shows the tight coordination of DA and ions in the OF*c** state.

Occurrence of *Holo-Occluded* State

The OF*c** state was stabilized only temporarily. Four independent aMD runs invariably showed that hDAT further progressed to a more stable occluded structure, the so-called *holo-occluded* state, which was comparable with that observed in the simulations of LeuT OF → IF transition (Cheng and Bahar, 2014). Two inter-helical distances distinguish the *holo-occluded* state from OF*o* and OF*c**, as illustrated in Figure 4: TM1b-TM10 and TM6a-TM10, both probing the extent of exposure to the cell exterior. A third metric, TM1a-TM6b, reflecting the exposure to the cytosol, did not exhibit any important change, indicating that while the EC-facing region contracts during these passages, the (originally closed) IC-facing TM1a-TM6b pair remains unchanged, hence the name *holo-occluded* whereby the ligand is "sealed" from both environments. Notably, these inter-helical packing properties, typical of the *holo-occluded* state, were not observed in the *apo* hDAT (Figure S3).

Furthermore, in contrast to OF structures, the EC vestibule is almost dehydrated in the *holo-occluded* state, and the closed IC face also prevents the hydration of the site S_1 (Figure 4B). A cluster of hydrophobic residues, W84 (TM1b), P387 (EL4b), and F472, L475, A479, and A480 (TM10), closely associate in this state (Figure 5) to obstruct water influx from the EC vestibule. Further data on time-resolved events associated with the transition to the *holo-occluded* state consistently observed in two independent runs can be seen in Figures 6 and S4. We note the gradual decrease in TM6a-TM10 and TM1b-TM10 distances and the minimal increase in TM1a-TM6b; the fluctuations in Cl^- position; and the formation of the salt bridge E428-K260 at the expense of E428-R445, releasing TM9 to assume a more "open" conformation.

Propensity of *Holo-Occluded* State to Transition into IF State

As the simulations proceeded in the *holo-occluded* state, we saw structural fluctuations signaling the propensity of this state to transition to the IF state. The intermittent dislocations of Na2 (see below) started to trigger the permeation of a few IC water molecules (Figures 6D and 7), which together with the disruption of the N82-N353 hydrogen bond near Na1 and Cl^- (Figure 7C) contributed to destabilizing the site S_1. We also note the outward tilting TM5 and TM9 accommodated by the extension of a TM4-TM5 loop (probed by G258-G263 distance increase from 8 to ~12 Å) (Figure S4). One might indeed qualify this intermediate between OF*c** and IF*o* as IF*c**, like the one resolved for MhsT (Malinauskaite et al., 2014). Yet other properties (in addition to TM1a-TM6b association) suggest an occluded, rather than an

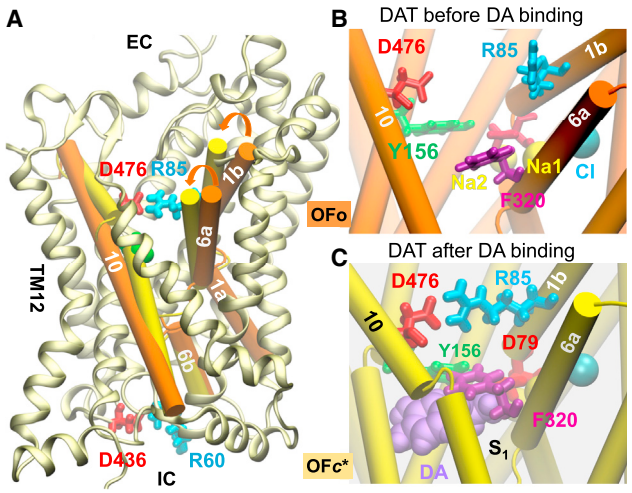

Figure 3. DA Binding to Site S_1 Prompts the Closure of EC Gates and Inward Tilting of TM1b, TM6a, and TM10, Leading to Outward-Facing Closed State

(A) MD-resolved hDAT in the outward-facing closed (OFc*) state (cream ribbons). Alignment of a representative OFc* conformation (yellow) sampled in MD simulations with the initial hDAT in the OF*o* state (orange) (RMSD ~1.9 Å).

(B) Substrate-binding pocket before DA binding, in the OF*o* state.

(C) Same pocket after binding. Isomerization of F320 brings its aromatic side chain on top of DA. Y156-F320 and salt bridge by R85-D476 serve as EC gates (see coordination of DA and ions in Figure S2).

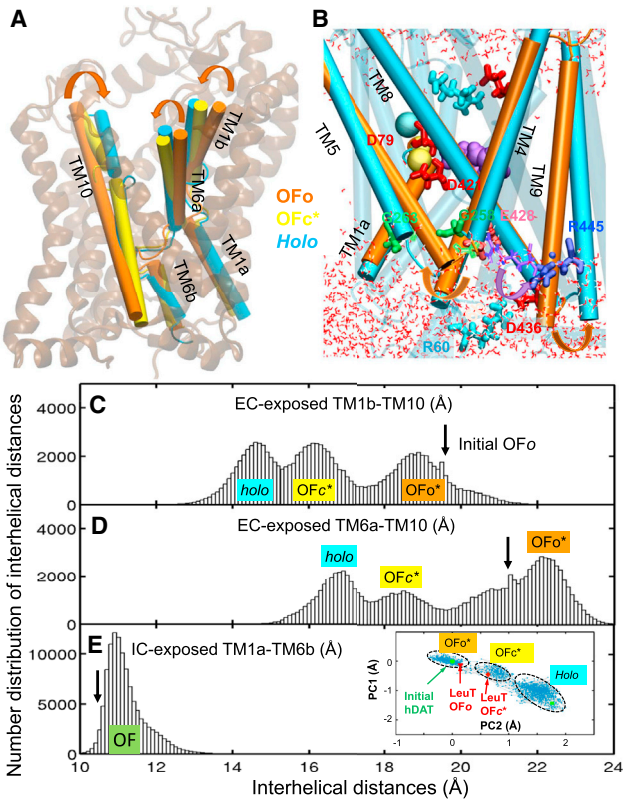

Figure 4. Characteristics of the *Holo-Occluded* State Stabilized during the Passage from OF to IF State, after DA Binding

(A) Structural alignment of MD-resolved OFc* (yellow; RMSD ~1.9 Å from OF*o*), *holo-occluded* (cyan; RMSD ~3.2 Å from OF*o*) and OF*o* (orange) states. TM1b, TM6a, and TM10 helices probe EC exposure.

(B) TM5 and TM9 reorientations during OF*o* → *holo-occluded* transition. In the *holo-occluded* state, the binding site is dehydrated (water molecules in red).

(C–E) Histograms of inter-helical distances for (C) TM1b-TM10, (D) TM6a-TM10, and (E) TM1a-TM6b, based on 110,000 MD snapshots. The inset shows the snapshots projected onto the subspace spanned by principal components PC1 and PC2. Peaks at 19.0 ± 0.5, 15.9 ± 0.5, and 14.6 ± 0.5 Å in (C) characterize the TM1-TM10 distances in *holo-occluded*, OFc*, and OF*o* states, respectively. Corresponding TM6a-TM10 peaks are 22.4 ± 0.5, 18.5 ± 0.5, and 16.9 ± 0.5 Å in (D). TM1a-TM6b distances (at the IC-facing region) remain closed at 11.2 ± 1.0 Å. See the histograms obtained for the *apo* hDAT in Figure S3.

IF, state, e.g. the persistence of the IC-gating salt bridge R60-D436 and the tri-aromatic interactions W63-F332-T335 (counterpart of LeuT W8-Y265-Y268), which would restrict, if not block, access of IC water, a feature typical of OF state (Kniazeff et al., 2008; Loland et al., 2004); the stable coordination of DA, Cl^-, and Na1.

Dislocation of Na2 and IC Water Permeation Push TM5 Open

In the hDAT OF*o* state, Na2 was coordinated by the carbonyl of the highly conserved G75 and V78 (TM1) and L418 (TM8) and side chains of D79, S422, and D421. Upon DA binding and reconfiguration into the OFc* and then *holo-occluded* states, S422 and D79 side groups rotated to interact with DA, leading to weaker interactions with Na2. Na2 instead found a new partner, T269 from TM5 (Figure S2). While the binding pocket was generally dehydrated in the *holo-occluded* state, transient IC water wires occasionally formed during the aMD runs. These, together with the increased fluctuations and momentary dislocations of Na2 (Figure 6 and S4), triggered the permeation of additional water molecules (Figure 7) and led to a kinking of TM5 near T269-P273 and its opening to further expose S_1 to the IC aqueous medium.

Opening of the IC Vestibule

hDAT progressed to IF*o** state in two independent runs (6 and 11; Figures S5 and S8, respectively; see Movies S1 and S2 for the OF*o** → *holo-occluded* → IF*o** transition that proceeded by similar patterns in both runs). IC water molecules accessed in both runs the vicinity of DA and Na1 to destabilize the S_1 and the hydrophobic cluster W63-F332-Y335. Na2 dislodging promoted, if not preceded, the concerted reorientations of TM helices and disruption of salt bridges R60(TM1)-D436(TM8) and K66(TM1)-R345(TM7), which would "release" TM1a that tilted outward. The local destabilization effects propagated to the IC-exposed parts of TM1a, TM7 and TM8. TM1a outward tilting gradually became more pronounced, which drove further influx (and steady occupancy) of water. DA rotated downward toward the IC entrance (Figures 8E and S5E) as the F76 side chain (Figure S2A) swung away from S_1.

Release of Ions and Substrate

The reorientations of TM1a and TM7 broke the hydrogen bond N82-N353 between these helices (Figure 7). N82-N353 was a stabilizing interaction near the binding pocket. Its disruption gave rise to an enlargement in the cavity near Na1 and Cl^-, which

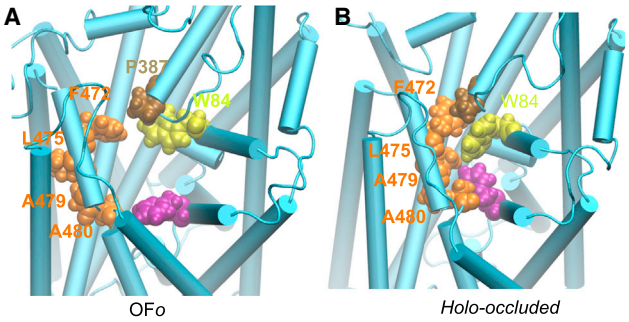

Figure 5. Hydrophobic Core Formed in the *Holo-Occluded* State near the EC Vestibule

(A) Orientations of W84 (TM1b), F472, L475, A479, and A480 (TM10) in the OF*o* conformation, and (B) their close packing near F320 (TM6a; purple) in the *holo-occluded* state. Snapshots were taken from run 9. The swinging of W84 toward the center was consistently observed in all aMD runs that sampled the *holo-occluded* state.

led to the release of Na1 and Cl^- (Figure 8D). Strikingly, TM5 outward tilting coupled with TM1a opening induced the formation of an IC pore, consistent with that observed in IF*o* LeuT crystal structure (Figure 9) as well as our recent LeuT simulations (Cheng and Bahar, 2014). The same pore allowed for the exit of Na1 and Cl^- (and DA; see below) to the cytosol (Figure 8F). The exit of Na2 and DA, however, was prevented by the electrostatic attractions with D79 and D421, even though the IC vestibule reached a wide-open conformation in runs 6 and 11 (Figures 8E and S5E).

We hypothesized that DA release required (1) a weakening of the attractions by D79 and D421 upon their protonation, for example, or (2) the occupancy of the IC exit by negatively charged entities (i.e. phosphorylation or negatively charged residues clustered along the pore). To test the first hypothesis, we protonated D79 in silico to observe whether the elimination of the attractive interactions between the oppositely charged D79 and DA would facilitate the dislocation of DA. Note that D79 was surrounded by hydrophobic residues F76, A77, V78, L80, A81, W84, F320, and L418, and had access to IC water, which further suggested that it might be protonated. Two independent runs starting from the IF*o** state indeed showed that DA diffused within 50 ns (run 12) and 20 ns (run 13) to the IC region upon protonation of D79 (but not D421) (Figure 8). The release path for Cl^-, Na1, and DA was the same (Figure 8F). Weak attractions by series of negatively charged residues lining the pore (D436, E437, E446, and E126) presumably guided, but did not detain, the DA transported.

Global Transitions Mapped by Principal Component Analysis

Principal component analysis (PCA) of the trajectories generated in the present study was performed using ProDy (Bakan et al., 2014). Figure S6 shows the projections of snapshots from eight runs onto the resulting principal space, spanned by PC1 and PC2. These two principal modes account for >45% of all motions. The passage over three global states OF, *holo-occluded*, and IF is clearly seen as the result of two principal modes of reconfiguration. Further analysis of runs 6 and 11 is presented in Figure 10A, which again highlights the three distinctive states also shown as a probability distribution (lower panel). Collective movements along PC1 and PC2 are illustrated in Figure 10B. The EC-exposed helices (upper panels) display inward tilting to shrink the EC vestibule in both modes, while the IC-exposed regions open up, consistent with the OF → IF transition.

DISCUSSION

Summary of Findings

Our simulations permitted us to visualize for the first time the complete sequence of events from recognition of DA from the EC region to its intake into the presynaptic cell, preceded by the release of Na1 and Cl^-. The observed (and proposed) transport mechanism is summarized in Figure 10C, and Movie S3 displays the complete process. Upon DA binding to S_0 and then S_1 in the OF*o* hDAT, the EC-exposed TM1b and TM6a undergo 10°–15° inward tiltings, coupled to the closure of EC gates R85-D476 and Y156-F320, leading to the OF*c** state (Figure 3); this relatively short-lived state spontaneously proceeds to a more compact conformation, whereby the DA/ion binding site is secluded from both the EC and IC environments: the *holo-occluded* state. Inward tilting of TM10 and association with TM1b promotes the formation of a hydrophobic cluster (Figure 5)

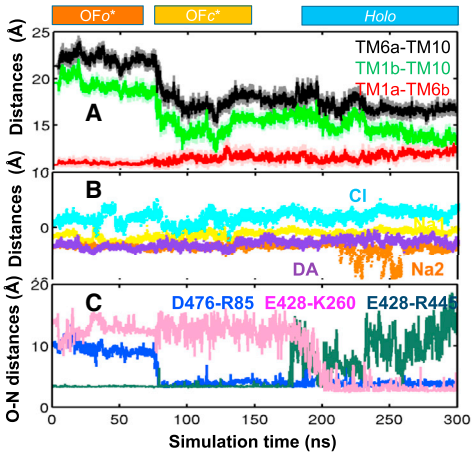

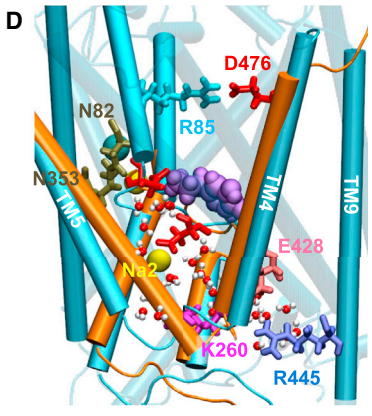

Figure 6. Destabilization of Na2, TM5 Tilting, and IC Water Permeation during the Transition from OF*c to *Holo-Occluded***

(A–C) Time evolutions of (A) inter-helical distances, (B) z positions of DA and ions, and (C) O-N distances indicating salt bridge switches.

(D) Snapshot at 220 ns shows the influx of IC water coupled to the outward tilting of TM5 (from its OF*o**/OF*c** (orange) to its *holo-occluded* (cyan) orientation) and the disruption of the salt bridge E428-R445 at the IC vestibule entrance, succeeding the temporary dislodging of Na2 toward the IC vestibule. These changes indicate the predisposition of the *holo-occluded* structure to proceed toward the IF state (Figure 8).

For more details see Figure S4.

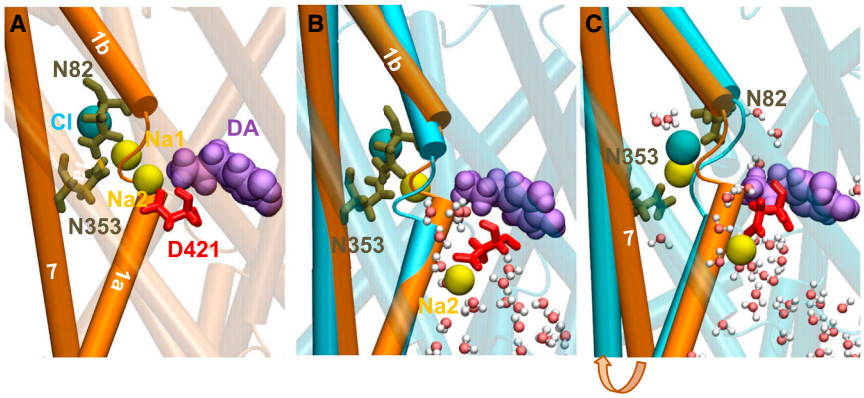

Figure 7. Concerted Motions of TM1 and TM7, Accompanied by the TM1a-TM1b Loop Reordering, Break the Hydrogen Bond between N82 and N353 and Facilitate the Release of Na1 and Cl⁻

(A) In the typical OF*o* state (orange), N353 (TM7) and N82 (TM1b) form a hydrogen bond, with Na1 and Cl⁻ located in close vicinity.

(B) The transition to *holo* state (cyan) involves the intermittent hydration of the binding site, by IC water, driven by Na2 dislocation. The hydrogen bond between N353 (TM7) and N82 (TM1b) prevents further penetration of the water molecules.

(C) Disruption of the N353-N82 hydrogen bond is driven by the reorientation of TM1a and b, and TM7, enabled by the disordering of the kink between TM1a and TM1b.

preventing the hydration of S_1 (and evidently the escape of DA and ions back to the EC region). TM10 tilting also alters the orientation of the connected TM9, which promotes a weakening in interactions among the IC-exposed TM helices; for example, R445-E428 and E446-K257, which connect TM9 to TM8 and TM4 in the OF state, are disrupted. Unwinding of the TM4-TM5 loop (G258-G263) permits the opening of TM5 to the IC region, promoted by Na2 dislocations and permeation of IC water molecules. Subsequently, significant TM1a outward tilting breaks the salt bridges K66-D345 and R60-D436 to complete the transition to IF state and release Cl⁻ and Na1 (Figures 8 and S5) facilitated by the disruption of the N82-N353 hydrogen bond (Figure 7). D79-DA interaction appears to be the only remaining barrier to the release of DA, which is realized only in the protonated state of D79.

In addition to these biological findings, the present study has methodological implications. The dual-boost aMD simulations (Hamelberg et al., 2007; Miao et al., 2013) of hundreds of nanoseconds are shown here to successfully sample long-time events well beyond the scope of cMD. Indeed, hundreds of aMD trajectories have been shown to capture events at the milliseconds time scale (Pierce et al., 2012). The advantages of dual-boost aMD are obvious. First, there is no need for a priori definition of the targeted directions of changes (Markwick and McCammon, 2011). Second, dual-boost aMD not only samples local side-chain reconfigurations efficiently, but also the global

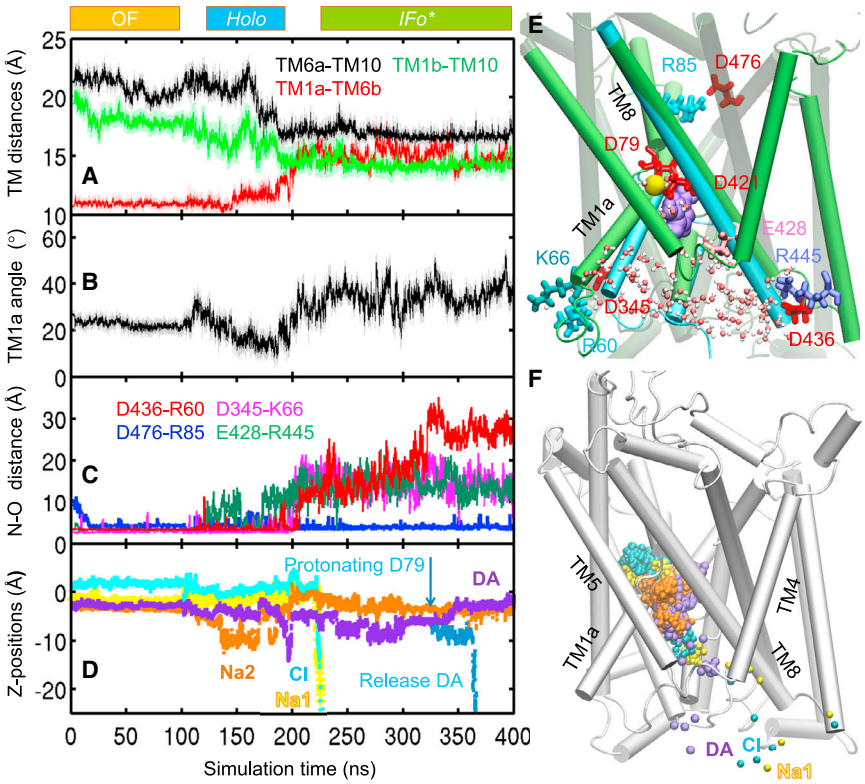

Figure 8. Time-Resolved Events During the Transition of hDAT from OF*o to *Holo-Occluded* to IF*o** to IF*o***

(A) Gradual closure of EC-exposed TM1b-TM10 and TM6a-TM10, and concurrent opening of the IC-exposed TM1a-TM6b.

(B) TM1a tilting relative to membrane normal (z axis).

(C) Disruption of the IC-facing salt bridges D436-R60 (IC gate), E428-R445, and D345-K66, and early formation and persistent stability of the EC-gating D476-R85.

(D) Z positions of DA, Na1, Cl⁻, and Na2. Note the instability of Na2 around 150 ns, which triggers the succeeding events. Na1 and Cl⁻ leave the transporter while Na2 and DA remain bound. An alternative trajectory for DA (blue) was generated after protonating D79 (run 12), which led to its release.

(E) An IF*o** conformation (green; snapshot at 325 ns) and reorientations of TM1a and TM8 relative to their *holo-occluded* (cyan; 150 ns) pauses.

(F) Exit pathway of DA (purple dots), Cl (cyan dots), and Na1 (yellow dots). Na2 (orange dots) remains bound. The pore is lined by TM1a, TM6b, TM8, and TM5. Data refer to 300-ns aMD (run 11) preceded by 100-ns cMD (run 8).

See also Figure S5.

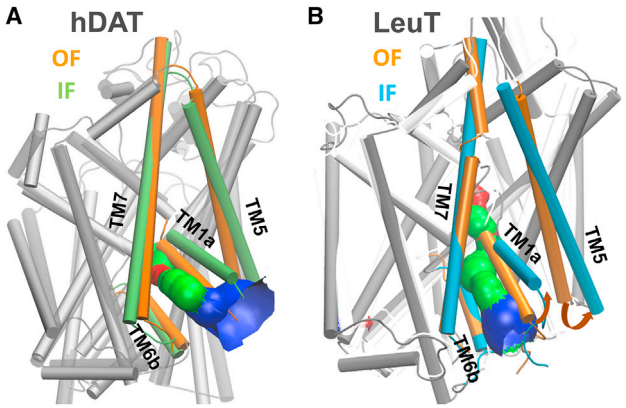

Figure 9. TM5/TM7 Outward Tilting Coupled with TM1a Tilting Facilitates the Formation of the IC Pore for Release of Substrate/Sodium Ions

(A and B) Alignment of snapshot in the hDAT IF conformation with the initial hDAT OF*o* (white transparent) (A); and alignment of the LeuT IF conformation with the initial LeuT OF*o* (white transparent) (B). For hDAT, TM1a, TM5, TM6b, and TM7 are highlighted in pale green (IF) and orange (OF). For LeuT, TM1a, TM5, TM6b, and TM7 are highlighted in blue (IF*o*; PDB: 3TT3) and orange (OF*o*; PDB: 3TT1). The snapshot of hDAT OF and IF conformation is taken from the energy minimized OF*o* conformation and the last frame in run 12. The IC pores were plotted using HOLE (Smart et al., 1996).

transitions, in contrast to the dihedral-boost aMD that may fail to capture global changes (Cheng and Bahar, 2013). The approach used here may be advantageously employed in future investigations of transport or other complex phenomena at the full-atomic scale.

Comparison with Experimental Data for LeuT-Fold Family Members

Many events observed here for hDAT are consistent with those inferred from LeuT structures in different states (see Figure 9) (Krishnamurthy and Gouaux, 2012; Yamashita et al., 2005) or from LeuT simulations (Cheng and Bahar, 2013, 2014). Essentially, global movements (concerted reorientations of TM helices) are conserved. Local interactions such as EC-/IC-gating mechanisms also share close similarities, while the identity of residues that take on comparable roles is specific to the transporter. Thus, the overall fold (or architecture) dictates the global motions, which in turn defines the transport mechanism. However, substrate specificity is imparted by sequence dissimilarities or insertions. We can learn about shared mechanisms from family members, notwithstanding the need to examine individual members to learn about their specific features.

Notably, new structural data were recently reported for dDAT in the presence of DA and psychostimulants (Wang et al., 2015). The DA binding pose and site predicted here for OF hDAT (Figure 1B) show good agreement with those observed in the OF crystal structures. Our simulations further show that DA binding to site S_1 triggers a closure of the EC vestibule. The resulting conformer, OFc*, shares close similarities with the Leu-bound OF LeuT (Yamashita et al., 2005) (Figure 3). It is interesting to note that a similar closure of the EC vestibule is temporarily sampled even in the *apo* form of the transporter (runs 14–17; Figure S3). This is consistent with the view that the transporter has an intrinsic ability to sample open and closed forms, even prior to substrate/ligand binding; and ligand binding stabilizes one of the pre-existing forms (Bahar et al., 2015), here the closed form. The multiple *apo-closed* states resolved for the hDAT structural homolog betaine transporter (BetP) (Perez et al., 2012) further corroborate the accessibility of closed conformations in the *apo* state.

The structural transitions revealed by the present simulations can be further compared with mutagenesis and structural data on hDAT and its structural homologs. We enumerate below observations made here, which correlate with those made for hDAT or other transporters that share the LeuT fold.

1. Closure of two EC gates R85-D476 and Y156-F320 (Figure 3) is essential to the progression of hDAT from OF to IF states. The hDAT R85D mutant was recently shown to exhibit a complete loss of function, which was restored by the compensating mutation R85D/D476R (Pedersen et al., 2014). Furthermore, the mutation of Y156 to Ala or Cys led to hDAT inactivation (Beuming et al., 2008), and the mutation of F319 (counterpart of hDAT F320) in the orthologous rat DAT reduced the turnover rates for DA to less than 1,200-fold (Lin et al., 1999).
2. D79 plays a key role in DA uptake and stabilization, Na1 coordination, and succeeding structural transitions (Figures 2, S1, 4B, 6D, S4E, 8E, and S5E). Mutations of D79 to Ala, Gly, or Glu have been reported to significantly reduce DA uptake (Kitayama et al., 1992). The fact that even D79E reduces DA uptake suggests that not only the charge but also the size of the amino acid at position 79 is important in mediating DA translocation (Kitayama et al., 1992).
3. The *holo-occluded* state newly identified here for hDAT shows close resemblance to the occluded IF structure of MhsT from *Bacillus halodurans* recently resolved in the presence of Na^+ and L-Trp (Malinauskaite et al., 2014). In particular, the hydrophobic cluster centered on W84 (Figure 5) is strikingly similar to that revealed by MhsT crystal structure. The complete closure of EC vestibule prior to exposure of the IC vestibule is another feature common to both structures.
4. The dislocation of Na2 was noted here to trigger the transition of hDAT to substrate-releasing state (Figures 6B, 7, 8D, S4B, and S5D). This role of Na2 was also proposed for MhsT by Nissen and co-workers (Malinauskaite et al., 2014), and suggested by the computational study of LeuT dynamics by Zhao and Noskov (2011).
5. TM5 and TM10 reorientations facilitate the transition OF → IF. This parallels the observation for LeuT-fold family member BetP (Perez et al., 2012) as well as our recent study of LeuT transport cycle (Cheng and Bahar, 2014). Solvation through the TM5 pathway was also pointed out to facilitate the transition of MhsT to the inward-open state (Malinauskaite et al., 2014). The unwound part of TM5 in the conserved region GX_9P (G171-P181) of MhsT has been proposed (Malinauskaite et al., 2014) to trigger the solvation of Na2. We have not observed significant disordering at the hDAT homologous region, G263-P273, on TM5, but an extension of the IC-exposed loop G258-G263

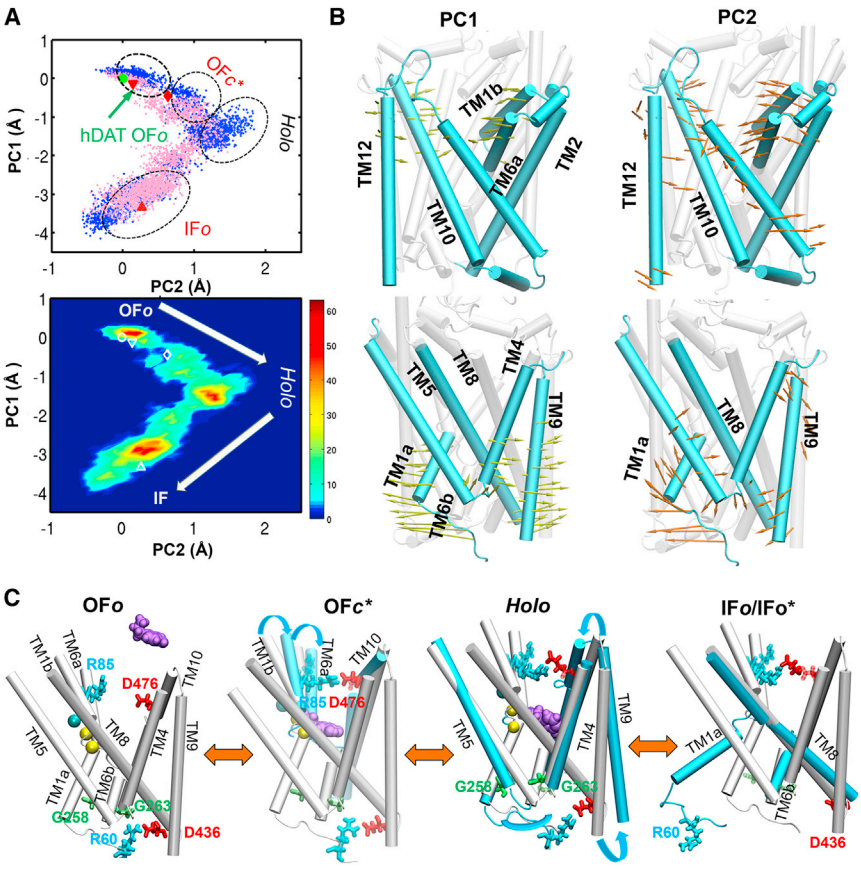

Figure 10. hDAT Trajectory from Outward-Facing Open to Inward-Facing Open State, via *Holo-Occluded* State, Visualized by Projecting the Trajectories onto the Subspace Spanned by Two Principal Components PC1 and PC2

(A) Snapshots from runs 6 (blue) and 11 (pink) projected onto the PC1-PC2 subspace (top); and their probability distribution (bottom), where three discrete global states OF, *holo-occluded*, and IF can be clearly seen (red regions). See also Figure S6.

(B) Movements along PC1 (yellow arrows) and PC2 (brown arrows).

(C) Conformation states visited by hDAT along with substrate translocation. Four states are distinguished by global helical motions (cyan) together with local conformation switches.

(Figures 4B and S4). This opening was the consequence, rather than the driving force, of the influx of IC water that was "attracted" by the dislodged Na^+.

6. TM1a outward tilting (Figures 8, S5, 9, and 10) is known to be a prominent feature in the IF state of LeuT-fold family of transporters (Krishnamurthy and Gouaux, 2012). TM1a has been pointed out to take part in a network of interactions that regulates IC gating (Kniazeff et al., 2008). In fact, the salt bridges K66-D345(TM7) and R60-D436(TM8) and the hydrophobic interaction W63-Y335(TM6b) ensure IC gate closure (Kniazeff et al., 2008), as observed in the present study. Consistently, these two salt bridges and aromatic interaction were destabilized in the simulations of the transition to the IF state. Not surprisingly, hDAT mutations D345N and Y335A have been pointed out to shift the equilibrium toward the IF state (Loland et al., 2004).
7. Previous studies suggest that extracellular zinc binding likely stabilizes the OF state, thus inhibiting DA uptake (Loland et al., 1999; Norregaard et al., 1998; Stockner et al., 2013). It has been also reported that zinc potentiates an uncoupled Cl^- conductance associated with DAT (Meinild et al., 2004) and is able to restore the transport function of hDAT in the Y335A mutant (Loland et al., 2002). Three amino acids were originally indicated to coordinate zinc binding (Loland et al., 1999; Norregaard et al., 1998): H193 (in EL2), and H375 and E396 (in EL4). Recently, the fourth zinc-binding residue D206 (in EL2) was identified and experimentally verified by Stockner et al. (2013). Notably, our modeled EL2 loop adopted as the initial conformation indicated that H193 and D206 would be in close proximity to H375 and E396 (Cheng et al., 2015) to form a putative zinc-binding site. Yet we note that due to the flexibility of the modeled EL2 loop, the putative zinc-binding pocket may be destabilized in the simulations. Further refinement of the EL2 loop using structurally important features deduced from previous studies (Stockner et al., 2013) may help.

Testable Hypotheses for Future Work

We present here a few examples of testable hypotheses on the role of particular residues in hDAT function. Stretching of the IC loop (G258-G263) between TM4 and TM5 may be prevented by mutating G258 and G263 to less flexible residues that may impair the reconfiguration of this loop, and thus interfere with the opening of TM5 to open the IC pore for DA/ions discharge to the cytosol. In addition to TM5, TM7 and, in particular, N353 on TM7 interacting with N82 (TM1), assist the transition to IF state, in a chloride-dependent mechanism (Figures 7 and 9), which would not be detected in structural homologs that lack anion co-transport. It would be interesting to test whether mutations of N353 and N82 to hydrophobic residues would affect anion transport. Moreover, the disruption of the salt bridges K66-D345 and R60-D436 was instrumental to releasing TM1a (Figures 8 and S5). Mutations of these residues to Ala would shift the equilibrium toward IF state, perhaps promoting the efflux, rather than influx, of DA/ions. Conversely, cysteine substitutions at those positions in the presence of reducing agents that promote their cross-linking may arrest the transporter in the OF state, which would promote binding from the synapse, but not uptake. Finally, here we report an IC-exposed salt bridge, R445-E428, for the first time to our knowledge, to facilitate the opening (or stabilize the open state) of the IC vestibule. This charged pair is highly conserved among the eukaryotic family

members, but is absent in LeuT. It remains to be seen whether substitutions (of alanines, for example) at those positions affect function.

Finally, we note that a large portion of the N and C termini have not yet been resolved for DAT. A recent study has proposed an approximate structural model for the (largely unstructured) N and C termini in the closely related serotonin transporter (Fenollar-Ferrer et al., 2014). Further studies are required to establish the role of N and C termini in assisting dopaminergic signaling.

EXPERIMENTAL PROCEDURES

Homology Modeling and Docking Analysis

Homology models of hDAT in the OF*o* state were constructed using MODELLER v9.10 (Sali and Blundell, 1993), based on dDAT crystal structure (PDB: 4M48) (Penmatsa et al., 2013). Sequence alignment was generated using Uniprot (http://www.uniprot.org). To model the human counterpart of the EL2 loop segment (S190 to P212 in hDAT) that was deleted in the crystal dDAT, we adopted the disulfide bridge between C180 and C189 in hDAT as a structural constraint (Stockner et al., 2013) in our homology modeling. Then 100 homology models were constructed, and the one with the lowest MODELLER objective function score was selected for further refinement and simulations. The quality of the modeled EL2 loop was assessed based on three criteria (Stockner et al., 2013): (1) the N-glycosylation sites N181, N188, and N205 were required to be exposed to the EC medium; (2) C180 and C189 would form a disulfide bond; (3) H193 would be in close proximity to H375 and E396 (in EL4) since a zinc ion is known to be coordinated by these three residues. The modeled EL2 loop adopted in the initial conformation satisfied all these three criteria (data not shown). Due to its high flexibility, EL2 was generally observed to be disordered during the course of simulations. DA docking simulations were performed using AutoDock (Morris et al., 2009) with the hDAT OF*o* model. The most favorable DA binding pose identified by AutoDock was observed to closely correspond to the site S_1, equivalent to that of Leu in LeuT OF*c** structure (PDB: 2A65) (Yamashita et al., 2005).

Preparation of Simulation Systems

The MD simulation systems were prepared using VMD (Humphrey et al., 1996). Figure 1 shows the simulation setup adopted as starting point in two sets of runs: (A) hDAT in OF*o* state, with one DA molecule placed more than 20 Å away from D79 (runs 1–6; see Table S1) and (B) hDAT in OF*o** state, where DA is pre-docked onto the site S_1, as the best predicted site by AutoDock (runs 7–13). Except for the position of the initial DA molecule, both systems were identical prior to simulations. Two sodium ions, one chloride ion and cholesterol molecule resolved in the crystal structure (not shown), were also included (Penmatsa et al., 2013). The TM domain of hDAT was inserted into the center of a pre-equilibrated palmitoyloleoylphosphatidylcholine (POPC) lipid mixture, following a previous approach (Cheng and Bahar, 2013, 2014). Fully equilibrated TIP3 waters were added to form a rectangular box of $104.6 \times 104.6 \times 150$ Å^3. Na^+ and Cl^- ions corresponding to a 0.15 M solution were added to neutralize the system. Overall the simulation system was composed of one hDAT, 196 POPC, 88 Cl^- ions, 83 Na^+ ions, two Zn^{2+} ions, four cholesterol molecules, and about 29,100 water molecules: a total of more than 141,000 atoms. The two Zn^{2+} ions originally placed in the EC region bulk solution remained in the solution and did not bind to hDAT during simulations. A summary of the series of simulations is presented in Table S1. The cMD protocol is described in the Supplemental Experimental Procedures.

Accelerated MD Method and Parameters

aMD simulations were performed using dual-boost mode (Hamelberg et al., 2007; Miao et al., 2013) implemented in NAMD2 (Phillips et al., 2005; Wang et al., 2011). Accordingly, boost potentials are applied not only to the dihedral angles (with corresponding parameters being E_{dihed}, α_{dihed}) (Hamelberg et al., 2004), but also to the total potential of all atoms (E_{total}, α_{total}) in the system. The input parameters (E_{dihed}, α_{dihed}; E_{total}, α_{total}) were chosen based on Miao et al. (2013): $E_{dihed} = (1 + \lambda)\, V_{dihed\_avg}$ and acceleration factor $\alpha_{dihed} = \lambda V_{dihed\_avg}/5$, where V_{dihed_avg} is the average dihedral energy calculated from 20-ns cMD equilibration simulations and λ is an adjustable boosting parameter adopted to be $\lambda = 0.3$, in line with earlier work (Miao et al., 2013). Likewise, for the total potential and corresponding acceleration factor, we adopted the relations $E_{total} = V_{total\_avg} + 0.2N_{atoms}$ and $\alpha_{total} = 0.2N_{atoms}$, where V_{total_avg} is the average total potential energy calculated from the 20-ns cMD equilibration and N_{atoms} is the number of atoms in the system.

Trajectory Analysis

VMD (Humphrey et al., 1996) with in-house scripts was used for visualization and analysis. Calculations of inter-helical distances were based on residues K66–V78 (TM1a), L80–Q93 (TM1b), A308–L322 (TM6a), F326–Y335 (TM6b), and G467–G481 (EC-exposed TM10 segment). For RMSD calculations, hDAT residues R58 to E598 were used, excluding the structurally unresolved EL2 loop segment (S190–P212). For all cMD runs, the RMSD was 2.0 ± 0.3 Å (Figure S7A). In all aMD runs performed to explore the transition from the OF state, the helical bundle remained well packed and the observed RMSD (3.6 ± 0.6 Å) was comparable with those obtained for LeuT OF*o* and IF*o* crystal structures (Figure S7B), in support of the applicability of dual-boost aMD. The EL2 loop was highly mobile in the simulations (Figure S7E); including the entire EL2 loop in the calculations increased the RMSDs to 3.6 ± 0.6 Å in cMD runs and 5.0 ± 1.0 Å in aMD runs (Figure S7D). PCA of MD trajectories was performed using ProDy (Bakan et al., 2014) and visualized using its Normal Mode Wizard implemented in VMD. The PCA was conducted for 354 C_α atoms corresponding to TM helical domains, the TM4-TM5 and TM8-TM9 loops, and the N-terminal segment R60-K65.

SUPPLEMENTAL INFORMATION

Supplemental Information includes Supplemental Experimental Procedures, seven figures and one table and can be found with this article online at http://dx.doi.org/10.1016/j.str.2015.09.001.

AUTHOR CONTRIBUTIONS

M.H.C. performed simulations; M.H.C. and I.B. designed the project, performed data analysis and structure calculations, and wrote the paper.

ACKNOWLEDGMENTS

We gratefully acknowledge support from NIH grants 1P30DA035778-01A1 and 5R01-GM099738 to I.B., and the computing award from the NSF TeraGrid (TG-MCB130006) and the Anton machine (NIH P41GM103712).

Received: April 22, 2015
Revised: August 31, 2015
Accepted: September 6, 2015
Published: October 15, 2015

REFERENCES

Amara, S.G., and Sonders, M.S. (1998). Neurotransmitter transporters as molecular targets for addictive drugs. Drug Alcohol Depend. *51*, 87–96.

Bahar, I., Cheng, M.H., Lee, J.Y., Kaya, C., and Zhang, S. (2015). Structure-encoded global motions and their role in mediating protein-substrate interactions. Biophys. J. *109*, 1101–1109.

Bakan, A., Dutta, A., Mao, W., Liu, Y., Chennubhotla, C., Lezon, T.R., and Bahar, I. (2014). Evol and ProDy for bridging protein sequence evolution and structural dynamics. Bioinformatics *30*, 2681–2683.

Beuming, T., Shi, L., Javitch, J.A., and Weinstein, H. (2006). A comprehensive structure-based alignment of prokaryotic and eukaryotic neurotransmitter/Na^+ symporters (NSS) aids in the use of the LeuT structure to probe NSS structure and function. Mol. Pharmacol. *70*, 1630–1642.

Beuming, T., Kniazeff, J., Bergmann, M.L., Shi, L., Gracia, L., Raniszewska, K., Newman, A.H., Javitch, J.A., Weinstein, H., and Gether, U. (2008). The binding sites for cocaine and dopamine in the dopamine transporter overlap. Nat. Neurosci. *11*, 780–789.

Cheng, M.H., and Bahar, I. (2013). Coupled global and local changes direct substrate translocation by neurotransmitter-sodium symporter ortholog LeuT. Biophys. J. *105*, 630–639.

Cheng, M.H., and Bahar, I. (2014). Complete mapping of substrate translocation highlights the significance of LeuT N-terminal segment in regulating transport cycle. PLoS Comput. Biol. *10*, e1003879.

Cheng, M.H., Block, E., Hu, F., Cobanoglu, M.C., Sorkin, A., and Bahar, I. (2015). Insights into the modulation of dopamine transporter function by amphetamine, orphenadrine and cocaine binding. Front Neurol. *6*, 134.

Fenollar-Ferrer, C., Stockner, T., Schwarz, T.C., Pal, A., Gotovina, J., Hofmaier, T., Jayaraman, K., Adhikary, S., Kudlacek, O., Mehdipour, A.R., et al. (2014). Structure and regulatory interactions of the cytoplasmic terminal domains of serotonin transporter. Biochemistry *53*, 5444–5460.

Forrest, L.R. (2013). Structural biology. (Pseudo-)symmetrical transport. Science *339*, 399–401.

Forrest, L.R., and Rudnick, G. (2009). The rocking bundle: a mechanism for ion-coupled solute flux by symmetrical transporters. Physiology (Bethesda) *24*, 377–386.

Forrest, L.R., Zhang, Y.W., Jacobs, M.T., Gesmonde, J., Xie, L., Honig, B.H., and Rudnick, G. (2008). Mechanism for alternating access in neurotransmitter transporters. Proc. Natl. Acad. Sci. USA *105*, 10338–10343.

Gedeon, P.C., Indarte, M., Surratt, C.K., and Madura, J.D. (2010). Molecular dynamics of leucine and dopamine transporter proteins in a model cell membrane lipid bilayer. Proteins *78*, 797–811.

Guptaroy, B., Zhang, M., Bowton, E., Binda, F., Shi, L., Weinstein, H., Galli, A., Javitch, J.A., Neubig, R.R., and Gnegy, M.E. (2009). A juxtamembrane mutation in the N terminus of the dopamine transporter induces preference for an inward-facing conformation. Mol. Pharmacol. *75*, 514–524.

Hamelberg, D., Mongan, J., and McCammon, J.A. (2004). Accelerated molecular dynamics: a promising and efficient simulation method for biomolecules. J. Chem. Phys. *120*, 11919–11929.

Hamelberg, D., de Oliveira, C.A., and McCammon, J.A. (2007). Sampling of slow diffusive conformational transitions with accelerated molecular dynamics. J. Chem. Phys. *127*, 155102.

Huang, X., and Zhan, C.G. (2007). How dopamine transporter interacts with dopamine: insights from molecular modeling and simulation. Biophys. J. *93*, 3627–3639.

Humphrey, W., Dalke, A., and Schulten, K. (1996). VMD: visual molecular dynamics. J. Mol. Graph. *14*, 33–38.

Indarte, M., Madura, J.D., and Surratt, C.K. (2008). Dopamine transporter comparative molecular modeling and binding site prediction using the LeuT(Aa) leucine transporter as a template. Proteins *70*, 1033–1046.

Jardetzky, O. (1966). Simple allosteric model for membrane pumps. Nature *211*, 969–970.

Kantcheva, A.K., Quick, M., Shi, L., Winther, A.M., Stolzenberg, S., Weinstein, H., Javitch, J.A., and Nissen, P. (2013). Chloride binding site of neurotransmitter sodium symporters. Proc. Natl. Acad. Sci. USA *110*, 8489–8494.

Khafizov, K., Perez, C., Koshy, C., Quick, M., Fendler, K., Ziegler, C., and Forrest, L.R. (2012). Investigation of the sodium-binding sites in the sodium-coupled betaine transporter BetP. Proc. Natl. Acad. Sci. USA *109*, E3035–E3044.

Kitayama, S., Shimada, S., Xu, H., Markham, L., Donovan, D.M., and Uhl, G.R. (1992). Dopamine transporter site-directed mutations differentially alter substrate transport and cocaine binding. Proc. Natl. Acad. Sci. USA *89*, 7782–7785.

Kniazeff, J., Shi, L., Loland, C.J., Javitch, J.A., Weinstein, H., and Gether, U. (2008). An intracellular interaction network regulates conformational transitions in the dopamine transporter. J. Biol. Chem. *283*, 17691–17701.

Krishnamurthy, H., and Gouaux, E. (2012). X-ray structures of LeuT in substrate-free outward-open and apo inward-open states. Nature *481*, 469–474.

Lin, Z., Wang, W., Kopajtic, T., Revay, R.S., and Uhl, G.R. (1999). Dopamine transporter: transmembrane phenylalanine mutations can selectively influence dopamine uptake and cocaine analog recognition. Mol. Pharmacol. *56*, 434–447.

Loland, C.J., Norregaard, L., and Gether, U. (1999). Defining proximity relationships in the tertiary structure of the dopamine transporter. Identification of a conserved glutamic acid as a third coordinate in the endogenous Zn^{2+}-binding site. J. Biol. Chem. *274*, 36928–36934.

Loland, C.J., Norregaard, L., Litman, T., and Gether, U. (2002). Generation of an activating Zn^{2+} switch in the dopamine transporter: mutation of an intracellular tyrosine constitutively alters the conformational equilibrium of the transport cycle. Proc. Natl. Acad. Sci. USA *99*, 1683–1688.

Loland, C.J., Granas, C., Javitch, J.A., and Gether, U. (2004). Identification of intracellular residues in the dopamine transporter critical for regulation of transporter conformation and cocaine binding. J. Biol. Chem. *279*, 3228–3238.

Malinauskaite, L., Quick, M., Reinhard, L., Lyons, J.A., Yano, H., Javitch, J.A., and Nissen, P. (2014). A mechanism for intracellular release of Na by neurotransmitter/sodium symporters. Nat. Struct. Mol. Biol. *21*, 1006–1012.

Markwick, P.R., and McCammon, J.A. (2011). Studying functional dynamics in bio-molecules using accelerated molecular dynamics. Phys. Chem. Chem. Phys. *13*, 20053–20065.

Meinild, A.K., Sitte, H.H., and Gether, U. (2004). Zinc potentiates an uncoupled anion conductance associated with the dopamine transporter. J. Biol. Chem. *279*, 49671–49679.

Miao, Y., Nichols, S.E., Gasper, P.M., Metzger, V.T., and McCammon, J.A. (2013). Activation and dynamic network of the M2 muscarinic receptor. Proc. Natl. Acad. Sci. USA *110*, 10982–10987.

Morris, G.M., Huey, R., Lindstrom, W., Sanner, M.F., Belew, R.K., Goodsell, D.S., and Olson, A.J. (2009). AutoDock4 and AutoDockTools4: automated docking with selective receptor flexibility. J. Comput. Chem. *30*, 2785–2791.

Norregaard, L., Frederiksen, D., Nielsen, E., and Gether, U. (1998). Delineation of an endogenous zinc-binding site in the human dopamine transporter. EMBO J. *17*, 4266–4273.

Pedersen, A.V., Andreassen, T.F., and Loland, C.J. (2014). A conserved salt bridge between transmembrane segments 1 and 10 constitutes an extracellular gate in the dopamine transporter. J. Biol. Chem. *289*, 35003–35014.

Penmatsa, A., Wang, K.H., and Gouaux, E. (2013). X-ray structure of dopamine transporter elucidates antidepressant mechanism. Nature *503*, 85–90.

Perez, C., Koshy, C., Yildiz, O., and Ziegler, C. (2012). Alternating-access mechanism in conformationally asymmetric trimers of the betaine transporter BetP. Nature *490*, 126–130.

Phillips, J.C., Braun, R., Wang, W., Gumbart, J., Tajkhorshid, E., Villa, E., Chipot, C., Skeel, R.D., Kale, L., and Schulten, K. (2005). Scalable molecular dynamics with NAMD. J. Comput. Chem. *26*, 1781–1802.

Pierce, L.C., Salomon-Ferrer, R., Augusto, F.d.O., McCammon, J.A., and Walker, R.C. (2012). Routine access to millisecond time scale events with accelerated molecular dynamics. J. Chem. Theor. Comput *8*, 2997–3002.

Piscitelli, C.L., Krishnamurthy, H., and Gouaux, E. (2010). Neurotransmitter/sodium symporter orthologue LeuT has a single high-affinity substrate site. Nature *468*, 1129–1132.

Sali, A., and Blundell, T.L. (1993). Comparative protein modelling by satisfaction of spatial restraints. J. Mol. Biol. *234*, 779–815.

Shaikh, S.A., and Tajkhorshid, E. (2010). Modeling and dynamics of the inward-facing state of a Na^+/Cl^- dependent neurotransmitter transporter homologue. PLoS Comput. Biol. *6*, e1000905.

Shaw, D.E., Deneroff, M.M., Dror, R.O., Kuskin, J.S., Larson, R.H., Salmon, J.K., Young, C., Batson, B., Bowers, K.J., Jack, C.C., et al. (2008). Anton, a special-purpose machine for molecular dynamics simulation. Commun. ACM *51*, 91–97.

Singh, S.K., Piscitelli, C.L., Yamashita, A., and Gouaux, E. (2008). A competitive inhibitor traps LeuT in an open-to-out conformation. Science *322*, 1655–1661.

Smart, O.S., Neduvelil, J.G., Wang, X., Wallace, B.A., and Sansom, M.S. (1996). HOLE: a program for the analysis of the pore dimensions of ion channel structural models. J. Mol. Graph. *14*, 354–360.

Stockner, T., Montgomery, T.R., Kudlacek, O., Weissensteiner, R., Ecker, G.F., Freissmuth, M., and Sitte, H.H. (2013). Mutational analysis of the high-affinity

zinc binding site validates a refined human dopamine transporter homology model. PLoS Comput. Biol. *9*, e1002909.

Thomas, J.R., Gedeon, P.C., Grant, B.J., and Madura, J.D. (2012). LeuT conformational sampling utilizing accelerated molecular dynamics and principal component analysis. Biophys. J. *103*, L1–L3.

Vaughan, R.A., and Foster, J.D. (2013). Mechanisms of dopamine transporter regulation in normal and disease states. Trends Pharmacol. Sci. *34*, 489–496.

Wang, Y., Harrison, C.B., Schulten, K., and McCammon, J.A. (2011). Implementation of accelerated molecular dynamics in NAMD. Comput. Sci. Discov. *4*, 015002.

Wang, K.H., Penmatsa, A., and Gouaux, E. (2015). Neurotransmitter and psychostimulant recognition by the dopamine transporter. Nature *521*, 322–327.

Yamashita, A., Singh, S.K., Kawate, T., Jin, Y., and Gouaux, E. (2005). Crystal structure of a bacterial homologue of Na^+/Cl^--dependent neurotransmitter transporters. Nature *437*, 215–223.

Zhao, C., and Noskov, S.Y. (2011). The role of local hydration and hydrogen-bonding dynamics in ion and solute release from ion-coupled secondary transporters. Biochemistry *50*, 1848–1856.

Zomot, E., and Bahar, I. (2012). A conformational switch in a partially unwound helix selectively determines the pathway for substrate release from the carnitine/gamma-butyrobetaine antiporter CaiT. J. Biol. Chem. *287*, 31823–31832.

Zomot, E., Gur, M., and Bahar, I. (2015). Microseconds simulations reveal a new sodium-binding site and the mechanism of sodium-coupled substrate uptake by LeuT. J. Biol. Chem. *290*, 544–555.

